# A Novel Soft-Switching Multiport Resonant Converter for Auxiliary Loads in Electric Vehicle

**V. Rajeswari*, Nalin Kant Mohanty****

** Department of Electrical and Electronics Engineering, Sri Venkateswara College of Engineering, Sriperumbudur, Tamil Nadu, India-602105 (Tel: 7373979714; e-mail: rajibe31@gmail.com)*
*** Department of Electrical and Electronics Engineering, Sri Venkateswara College of Engineering, Sriperumbudur, Tamil Nadu, India-602105 (e-mail: nkmohanty@svce.ac.in)*

***Abstract**:* This article introduces a novel soft-switching Multi-Port Converter (MPC) utilizing dual sources with a common ground structure, providing a high voltage conversion ratio for electric vehicle applications. To reduce voltage stresses across all semiconductors and maintain continuous output current, a new switched Z-Quasi Resonant (S-ZQR) network is integrated with the conventional buck configuration. The key features of the ZQR network are reduced voltage stress on power components and improved voltage gain, particularly at low duty cycle ranges. Without adding any auxiliary circuit, the proposed topology provides low-stress characteristics, higher efficiency, a wide voltage range, and soft-switching conditions on the power switches, thereby achieving a maximum efficiency of 93.67%. Additionally, the configuration is designed and analyzed using a simple conventional controller with fewer components to achieve Zero-Current Switching (ZCS) at the lowest switching losses compared to recently reported converters. The theoretical and comparative analyses are performed to validate the converter performance using MATLAB/ Simulink under various operating conditions. In the laboratory, a 150W hardware prototype was developed, built, experimentally verified, and validated with the results.

*Keywords*: Battery; DC Load; Electric Vehicle; Multi-port; Non-isolated; PV source; Soft-Switching; ZCS

## 1. INTRODUCTION

In recent years, high-gain converter topologies have gained more prominence in various applications such as renewable energy systems, electric vehicle charging applications, DC micro-grids, BESS, and grid-integrated DC storage systems. Several research and development projects are undergoing for the implementation of new converters aiming at improved voltage conversion ratio, enhanced efficiency, better energy density, and so on. Particularly, integrating two or more converters, bidirectional, multiport topologies, and interleaved configurations has gained more interest among researchers. However, researchers are primarily focused on soft-switching techniques, which have been highlighted in various works of literature. Most of the configurations have adopted these techniques to improve converter efficiency and eliminate switching losses. This study briefly discusses various charging topologies and power electronics converter solutions applicable in electric vehicles (A. Ali et al., 2024). A quasi-resonant tank combining a three-winding coupled inductor (CI) to provide fully soft-switching conditions and solve EMI issues with low-order ripples (S. Abbasian et al., 2022). A multiport configuration combining a ZQR network provides higher voltage gain in electric vehicle charging applications, as reported in this study (N. Alajmi et al., 2021). This article introduces a multiport converter using fewer components, and its performance characteristics are compared with existing topologies (H. Aljarajreh et al., 2022). A dual switch arrangement comprises a switched inductor (SL) cell that is developed with a simple control technique for achieving higher gains (Bao et al., 2021). Various classifications, features, applications, and characteristics of power converters providing soft-switching conditions are described briefly in this article (X. -F. Cheng et al., 2021). A voltage multiplier cell (VMC) based diode clamp and switched capacitor (SC) cell are incorporated to provide ZVS, reducing switching losses, and improving the converter's efficiency using more components (M. R. S. de Carvalho et al., 2022). Mostly, interleaved Quasi-Resonant (QR) structures with energy storage systems are employed to improve the voltage conversion ratio at low voltage (LV) and high voltage (HV) sides (Z. Fang et al., 2021). Here, an approach triple-port converter (TPC) with coupled inductor technique and soft switching cell is introduced to improve the converter gain and achieve higher efficiency (R. Faraji et al., 2021). In (N. Hassanpour et al., 2023), the proposed structure employs a current-source topology enabling operation in both polarities, provides soft-switching conditions, as well as low current stress characteristics. A switched capacitor cell with a zero-voltage transition (ZVT) circuit is introduced (M. Heidari et al., 2022) for providing better soft-switching capability. To boost the system efficiency and achieve ZVS conditions, a bidirectional switched-capacitor structure is developed with different phase shift control techniques (L. He et al., 2022). Employing a battery switching cell with a single inductor structure is introduced for better energy transfer and flexibility (J. -Y. Kim et al., 2021). Furthermore, to alleviate reverse recovery problems, voltage stress and to achieve ZVS, a fly-back energy-fed voltage multiplier cell is presented (K. R. Kothapalli et al., 2021). A detailed comparative analysis of multi-port topologies employed in high-power applications was discussed elaborately in this study (Y. Li et al., 2022). The various topologies of achieving soft-switching characteristics in power converters to reduce switching and conduction losses have been presented (Maalandish et al., 2024). Here, a single magnetic core-based power converter is employed to achieve full ZVS and increase power density (M. Maghsoudi et al., 2024). This article focuses on advanced control methodologies, converter topologies in transportation electrification. Additionally, future developments, recent trends, and challenges arising in bidirectional converters are also discussed (Moumita Das, 2023).

This study presented various advanced topologies and new control techniques in multi-port converters briefly (Mudadla Dhananjaya, 2022). In (Patakamoori et al., 2023), an efficient soft-switched LED driver is suggested to improve efficiency and reduce ripples across the load current. But in renewable energy systems, an efficient multiport configuration with the switched capacitor cell providing common ground and ripple-less continuous current is suggested (S. Rostami et.al, 2022). A cuk-based power factor correction is introduced (Shameli et al., 2024) to eliminate harmonic distortion and achieve higher efficiency without adding an input filter. However, voltage multiplier-based boost converters are employed in real-time applications (P. Talebi et al., 2023) to mitigate switching loss and the diode reverse recovery problem of all switching devices. Here, isolation-based quasi Z-source converters are incorporated to decrease power loss, voltage spikes, and the leakage inductance of the transformer (G. Tian et al., 2024), which results in complexity in control. A bidirectional converter with zero ripple current cells is incorporated to achieve low switch stress, reduced ripple voltages, and higher output gain (Z. Wang et al., 2021). The various configurations of soft-switched topologies for non-isolated DC-DC converters are presented in detail in Fig. 1.

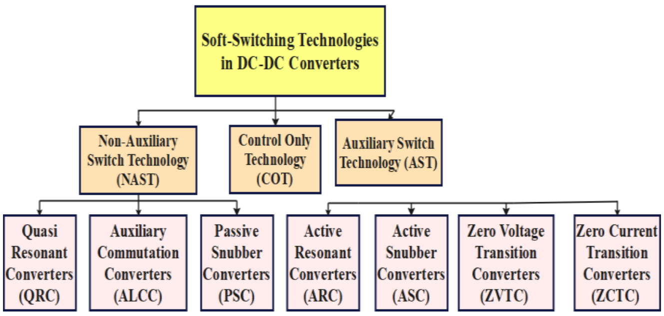


Fig. 1. Classification of Soft-Switching Technology.

To regulate power flow between battery, PV, and grids simultaneously, a differential power processing multiport topology is introduced for battery and PV integrated systems (J. Wang et al., 2022). In this approach, resonant-based coupled inductors and capacitors are integrated into an interleaved structure to achieve wide voltage ranges (F. Yuan et al., 2023). Furthermore, to minimize both switching and conduction losses, a converter with soft switching performance and direct power transfer capability is studied (M. Zareie et al., 2021). To convert current terminals into voltage terminals, an optimization technique is approached in a multiport bidirectional converter with higher efficiency (H. Zhang et al., 2022). In (Y. Zhang et al., 2023), an optimal design method based on VSF control is designed to attain soft-switching conditions and peak efficiency with reduced losses.

Based on the above literature surveyed, the proposed system introduces a new multiport (MPC) converter that uses dual sources and provides a common ground structure between the sources and load terminals to address the drawbacks and constraints of the existing converter shown in Fig. 2, in terms of isolation, components count, voltage gain, switching losses, soft-switching conditions, and efficiency. The conventional system integrates buck and bidirectional DC-DC converters using a battery switching cell, however not appropriate to achieve soft-switching conditions, reduce switching losses, and is not applicable for PV-based renewable systems.

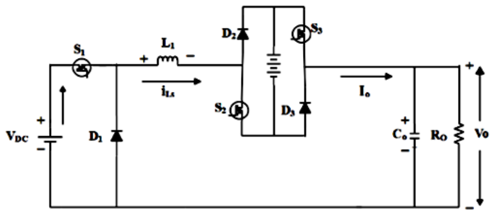

Fig. 2. Conventional system structure.

The concept of the proposed system is shown in Fig. 3. The converter's advantages include peak efficiency, better power density, and improved conversion ratio. This article proposes a new step-down converter incorporated with a switched Z-QR (Quasi Resonant) network that achieves soft-switching conditions under various operating modes from renewable energy systems (RES). The power from both sources satisfies the load requirement under various operating conditions.

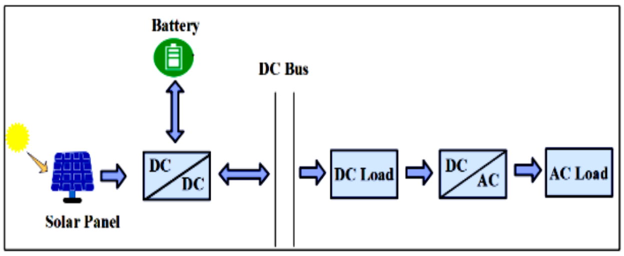


Fig. 3. Concept of Proposed System.

The proposed configuration connects both the battery source and the PV source to the load, where the PV system generates surplus power to the load due to an insufficient amount of energy in the battery. The proposed topology, as shown in Fig. 4, is developed into a step-down configuration followed by an S-ZQR converter powered with two input ports. Without adding any auxiliary circuit, the converter achieves fully soft switching conditions with reduced losses at low cost. The features of the converter promote a new framework for electric vehicle applications.

The notable features of the S-ZQR converter are as follows:

1. Achieves higher efficiency at all modes.
2. Sharing the same ground between sources and load terminals, which makes the system efficient.
3. Promotes a better voltage conversion ratio at a wide range of duty cycles.
4. Voltage and current stresses across semiconductor devices remain low.
5. Achieves soft-switching conditions at all modes.

In this article, the system configuration, performance, and features are organized into various sections. The operating principles at various modes were analyzed in Section 2. The design considerations and analysis were presented in Section 3. The system control strategy is detailed in Section 4. Simulation results and comparison with the existing converters are presented in Section 5. Experimental hardware results were presented in Section 6. Finally, the article conclusión is presented in Section 6.

## 2. PRINCIPLE AND OPERATING MODES OF CONFIGURATION

The proposed structure features dual source terminals with unidirectional and single bidirectional load terminals, all sharing a common ground. The multiport (MPC) converter includes a step-down converter followed by a switched Z-Quasi Resonant (S-ZQR) converter. The PV panel, along with battery sources, is connected to the DC load using a typical buck structure along with a ZQR converter. The configuration includes three active switches, and a simple control algorithm is incorporated to optimize the overall power converter. This architecture is well-suited for battery-PV-based DC systems. The multiport (MPC) system comprises three active-controlled switches ($S_1$,$S_2$,$S_3$), diodes ($D_1$,$D_2$), capacitors ($C_1$,$C_2$,$C_o$), and inductor coils ($L_1$,$L_2$,$L_3$). The system topology is shown in Fig. 4.

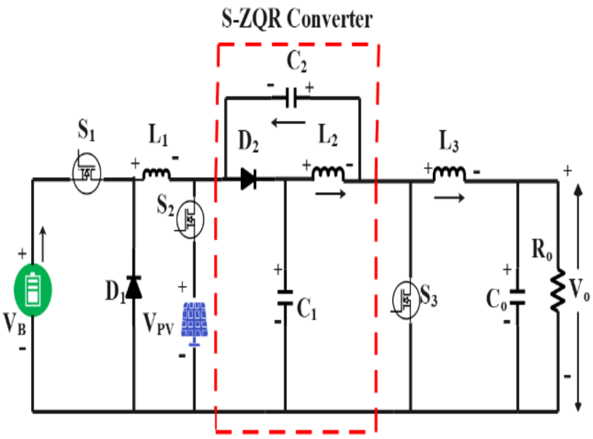


Fig. 4. Proposed System Topology.

The S-ZQR network includes ($C_1$, $D_2$, $C_2$, $L_2$). During the total switching period ($T_S$), the switches and diodes can conduct alternately. The MPC operates in both boost and buck modes, along with an S-ZQR network used to achieve soft switching conditions. The operating key waveform for the proposed MPC is shown in Fig. 5. The system utilizes two source terminals, PV and battery, where the output terminal serves as a common DC load. When both sources transfer energy to the load simultaneously, it is referred to as boost mode. In the buck state, only the load provides sufficient energy to the respective sources, referred to as RB mode. The operating waveform shown at mode 1 includes gate signals for $S_1$, $S_2$, $S_3$, the voltage across switches $S_1$, $S_2$, $S_3$, inductor currents $i_{L1}$,$i_{L2}$,$i_{L3}$, and diode current. The various modes of operation are explained in detail below.

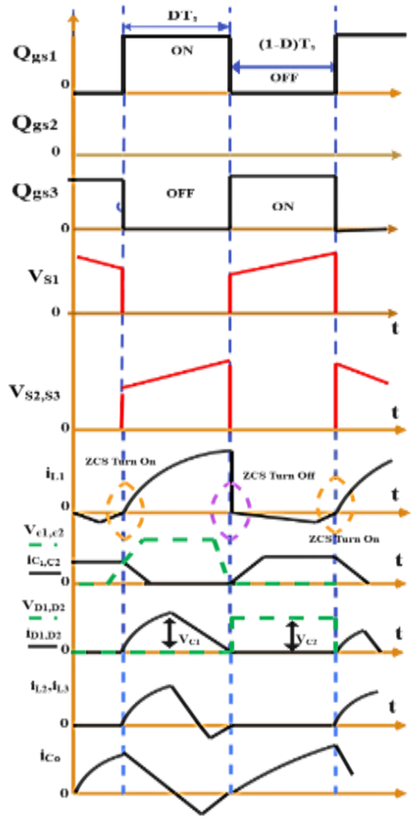


Fig. 5. The key waveform of the system at Mode 1.

### 2.1 Battery to Load (Mode 1-SISO)

During this mode, due to the unavailability of the PV source, the battery in maximum SOC alone transfers sufficient power to the DC load. To govern the output voltage $V_o$, switch $S_1$ alone is controlled and acts as a boost mode. The input current to the inductor $L_1$ achieves the ZCS condition. The two operating states of this mode are represented in Fig. 6.

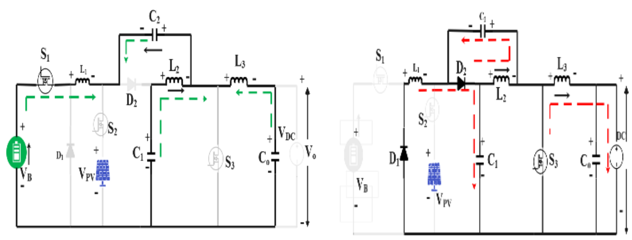

(i) (ii)

Fig. 6. Mode 1 (SISO) (i) State 1 (ii) State 2.

*(i) State 1 ($t_o$<T<$t_1$)*: Switch $S_1$ remains turned *ON* whereas, $S_2$, $S_3$ remain in the *OFF* state. The diodes remain in a reverse-bias condition. Here, the battery source and $C_2$ charge the inductor $L_1$. Therefore, $I_{L1}$=$I_B$+$I_{C2}$. $L_2$ also starts to charge through $C_1$, hence $I_{L2}$= $I_{C1}$. The capacitor $C_o$ is discharged to $L_3$ as shown in Fig. 6(i). Switch $S_1$ remains in the *OFF* state at $T$=$t_1$.

*(ii) State 2 ($t_1$<T<$t_2$)*: In this mode, $S_3$ is in *ON* state, while $S_1$, $S_2$ remains *OFF*. The diodes remain in a forward-bias state. The inductors $L_1$ and $L_2$ discharge their energy through $D_2$, $C_1$ to the DC bus as shown in Fig. 6(ii). The inductor $L_3$ also discharges its energy to the load.

### *2.2 PV Source to Load (Mode 2-SISO)*

During this mode, the PV source alone supplies its energy to the load, where the battery is available with a low SOC state. The switch $S_2$ is kept turned *ON* to supply sufficient solar PV power to the DC bus. The switching states at this mode are shown in Fig. 7.

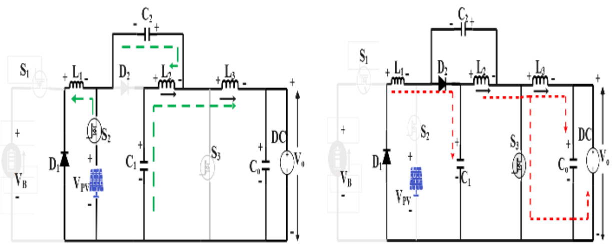

(i) (ii)

Fig. 7. Mode 2 (SISO) (i) State 1 (ii) State 2.

*(i) State 1 ($t_o<T<t_1$)*: $S_2$ is turned *ON*, where $S_1$ and $S_3$ are remains in *OFF* state. The PV source provides enough energy to supply inductor $L_1$, so that $I_{L1}= I_{PV} +I_{C2}$ and $I_{L2}=I_{C1}$ as shown in Fig. 7(i). This state ends at switch $S_2$ is in the *OFF* state.

*(ii) State 2 ($t_1<T<t_2$)*: In this state, $S_3$ remains *ON*, where $S_1$ and $S_2$ are turned *OFF*. $L_1$ discharges its energy through $D_2$ to charge $C_1$, and $L_2$ also discharges to the DC bus. The inductor $L_3$ charges through the load capacitor $C_o$ as shown in Fig. 7(ii). At $T=t_2$, $S_3$ is *OFF*.

### *2.3 PV and Battery to Load (Mode 3-DISO)*

In this mode, both the PV system and the battery source supply simultaneously to the DC bus (load). The four switching states are shown in Fig. 8. as follows.

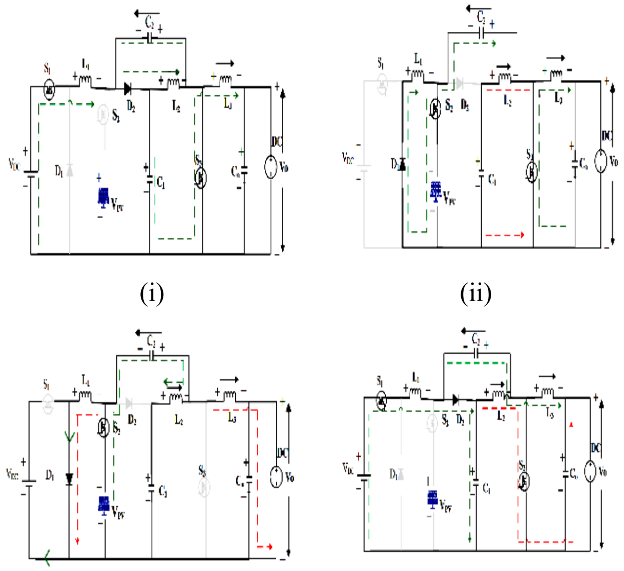

(i) (ii) (iii) (iv)

Fig. 8. Mode 3 (DISO) (i) State 1 (ii) State 2 (iii) State 3 (iv) State 4.

*(i) State 1($t_o<T<t_1$)*: $S_1$, $S_3$ are remains *ON*, where $S_2$ remains in *OFF* state. Hence, the battery alone supplies to charge $L_1$. Here, $C_2$ charges $L_2$ through forward-bias $D_2$. The inductor $L_3$ also charges through $C_1$ as shown in Fig. 8(i). At $T=t_1$, this state ends.

*(ii) State 2 ($t_1<T<t_2$)*: Here, $S_2$ and $S_3$ are turned ON, $S_1$ remains *OFF*. Inductor $L_1$ charges from the PV source, and $C_2$ also starts to get charged from the PV. Then, $L_2$ discharges through $C_1$ to load. The load capacitor also charges $L_3$ as shown in Fig. 8(ii).

*(iii) State 3 ($t_2<T<t_3$)*: $S_2$ is turned *ON* and $S_1$ and $S_3$ are remains *OFF*. $L_1$ discharges its energy into the battery through $D_2$, and PV source charges $L_2$ through $C_2$. Then, $L_3$ discharges to the DC bus as shown in Fig. 8(iii). At $T=t_3$, this state ends.

*(iv) State 4 ($t_3<T<t_4$)*: Here, $S_1$, $S_3$ are remains in *ON* condition, $S_2$ is turned *OFF*. Here, $L_1$ charges through the battery, and $C_1$ also gets charged. $L_2$ discharges its energy to the DC bus and $L_3$ charges through $C_2$ as shown in Fig. 8(iv). At $T=t_4$, this state ends.

### *2.4 PV to both DC bus and Battery (Mode 4-SIDO)*

During this mode, the PV source alone provides sufficient energy to both the battery and the load simultaneously. The switching states of this mode are shown in Fig. 9.

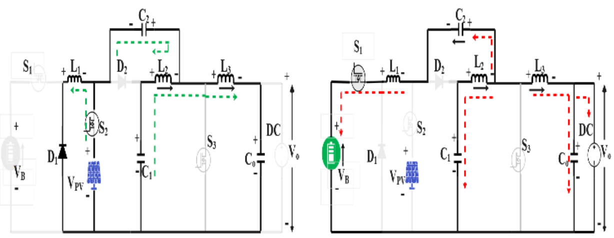

(a) (b)

Fig. 9. Mode 4 (SIDO) (a) State 1 (b) State 2.

*(i) State 1 ($t_o<T<t_1$)*: $S_2$ is *ON* and $S_1$, $S_3$ remains in *OFF* state. PV charges $L_1$ through $D_1$, while $L_2$ charges through $C_2$. Here, inductor $L_3$ starts to charge through $C_1$ as shown in Figure 9(i).

*(ii) State 2 ($t_1<T<t_2$)*: $S_1$ and $S_3$ are *ON*, $S_2$ remains in *OFF* state. Here, $L_1$ discharges into the battery, and $L_2$, $L_3$ also discharge their energy to the load as shown in Figure 9(ii). At $T=t_2$, the switching process ends.

### *2.5 Load to Battery (Mode 5-SISO (RB Mode))*

During this mode, PV panels are not able to supply sufficient power because of heavily shaded circumstances to both the DC load and the battery. So, the battery remains in a low SOC state. During this period, regenerative braking action takes place to transfer power from the DC bus (Load) to the battery, as depicted in Fig. 10. The switching states of this mode are explained below.

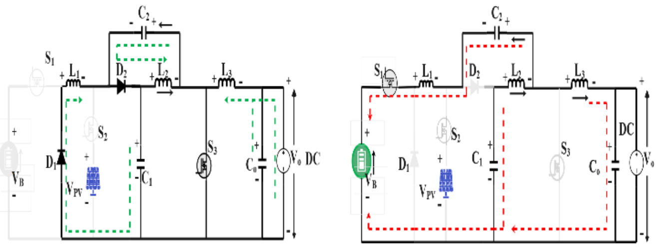

(i) (ii)

Fig. 10. Mode 5 (SISO) (i) State 1 (ii) State 2.

*(i) State 1 ($t_o$<T<$t_1$):* During this state, switch $S_3$ is *ON* and $S_1$, $S_2$ are turned *OFF*. Here, $L_3$ charges through the DC bus and load capacitor $C_o$, while $C_2$ starts to charge $L_2$. $D_1$, $D_2$ remain in a forward-bias state to charge $L_1$ through $C_1$ as shown in Fig. 10(i).

*(ii)State 2 ($t_1$<T<$t_2$):* $S_1$ is *ON* and $S_2$, $S_3$ are remains *OFF* state. Here, $L_2$ discharges energy into $C_1$ and the battery simultaneously. Meanwhile, $L_1$ discharges into the battery represented in Fig. 10(ii). At $T=t_2$, this state ends.

## 3. DESIGN CONSIDERATIONS

### *3.1 Inductor Design*

By applying the volt-sec balance principle and based on the current, the voltage across semiconductor devices, the inductors, and the capacitors is decided and designed.

Assuming 20% of the input ripple current, the minimum value of inductances is calculated as,

$$L_1 = \frac{(V_B - V_{C1})}{\Delta i_{L1} f_s} d_1 \quad (1)$$

$$L_2 = \frac{(V_{C1} - V_{C2})}{\Delta i_{L2} f_s} d_2 \quad (2)$$

$$L_3 = \frac{V_{DC}}{\Delta i_{L3} f_s} d_3 \quad (3)$$

Where $V_B$, $V_{c1}$, $V_{c2}$, $V_{DC}$, $d_1$, $d_2$, $d_3$, $\Delta i_{L1}$, $\Delta_{L2}$, $\Delta_{L3}$ are battery voltage, capacitor voltage, DC bus voltages, duty cycle, switching frequency ($f_s$), inductor coil current ripple, which operates under 20 kHz, respectively.

### *3.2 Capacitor Design*

By applying a charge-sec balance and assuming maximum voltage ripple, the minimum value of capacitances is calculated as,

$$C_1 = \frac{(1-d_1)(V_{PV} - V_B)}{R f_s \Delta V_{C1}} \quad (4)$$

$$C_2 = \frac{(d_2)(V_{PV})}{L_2 R f_s \Delta V_{C2}} \quad (5)$$

$$C_o = \frac{(1-d_1)(V_{DC})}{L_3 R f_s^2 \Delta V_{C1}} \quad (6)$$

$$\Delta V_{C1} = \frac{V_{in}(1-d)d}{R(1-d^2) f_s C_1} \quad (7)$$

$V_{PV}$, $f_s$, $R_o$, $d$ are the converter's PV voltage, switching frequency, load resistance, and duty cycle, respectively.

### *3.3 Voltage Conversion Ratio*

The system conversion ratios at modes 1, 2, and 5 are represented as,

$$M_1 = \frac{V_{DC}}{V_B} = D_{M1} \quad (8)$$

$$M_2 = \frac{V_{DC}}{V_{PV}} = D_{M2} \quad (9)$$

$$M_5 = \frac{V_B}{V_{DC}} = D_{M5} \quad (10)$$

Where $D_{M1}$, $D_{M2}$, $D_{M5}$ are modes 1, 2, and 5 duty ratios. The voltage conversion ratios of modes 3 and 4 with multiple inputs or outputs are represented as,

$$V_B = \frac{1}{K} V_{DC} = \frac{1}{K'} V_{PV} \quad (11)$$

Where K and K' are proportionality factors.

The voltage conversion ratios for mode 3 (DISO), based on volt-sec balance, are represented as follows:

$$M_{3,V_B} = \frac{V_o}{V_{DC}} = (1+K')D_{M3} \quad (12)$$

$$M_{3,V_{PV}} = \frac{V_o}{V_{PV}} = \left(1 + \frac{1}{K'}\right) D_{M3} \quad (13)$$

$$M_3 = \frac{V_o}{(V_B + V_{PV})} = D_{M3} \quad (14)$$

Similarly, by applying the volt-sec balance in mode 4 (SIDO), the voltage conversion ratios are expressed as follows,

$$M_{4,V_B} = \frac{V_B}{V_{PV}} \quad (15)$$

$$M_{4,V_O} = \frac{V_O}{V_{PV}} \quad (16)$$

$$M_4 = \frac{(V_B + V_O)}{V_{PV}} \quad (17)$$

### *3.4 Voltage and Current Stress Analysis*

All devices current and voltage stresses are calculated based on the inductor coil current and capacitor voltage parameters, respectively. However, $S_1$, and $S_2$ provide voltage stresses at a lower stage compared with conventional topologies, resulting in lower conduction losses. Since $V_{BAT}$ is higher than $V_O$ in the conventional converter, whereas in the proposed converter, $V_{BAT}$ and $V_{PV}$ are lower than $V_{DC}$. Therefore, the battery current and PV current are higher than the load current. Due to the presence of fewer components, the current stresses on all switches of the suggested topology can lessen the overall system power loss. The semiconductor components current and voltage stresses analysis are tabulated [24] shown in Table 1 below.

**Table 1. Voltage and Current Stresses.**

| Parameters | S1 | S2 | S3 | D1 | D2 |
|---|---|---|---|---|---|
| Voltage Stress | $V_B + V_{D1}$ | $V_{PV} + V_{C2}$ | $V_{C1} - V_{C2} + V_O$ | $V_B - V_{PV}$ | $V_{C1} + V_{DS2}$ |
| Current Stress | $I_B + I_{L1}$ | $I_{PV} - I_{L1} - I_{C2}$ | $I_O + I_{L3}$ | $I_B$ | $I_{PV}$ |

*3.5 Limitations of Port Voltages*

The nominal range of PV voltage can be expressed as [4],

$$V_{PV} = V_{DC} + \frac{V_B}{d}$$

At a 0.5 duty ratio, a DC bus voltage range of 24V, and a battery voltage of 12V, the PV system voltage are determined. The configuration operating modes are tabulated based on a several semiconductor devices used. The switching states at various modes are represented in Table 2.

**Table 2. Look up table of all modes of operation.**

| S.No | Modes | Type of Mode | States | $S_1$ | $S_2$ | $S_3$ | $L_1$ | $L_2$ | $L_3$ | $D_1$ | $D_2$ | $C_1$ | $C_2$ | $C_3$ | Output |
|---|---|---|---|---|---|---|---|---|---|---|---|---|---|---|---|
| 1. | Battery to DC bus | SISO | I | ON | OFF | OFF | ↑ | ↑ | - | OFF | OFF | ↑ | ↓ | ↓ | Buck |
| | | | II | OFF | OFF | ON | ↓ | ↓ | - | ON | ON | ↓ | ↑ | ↑ | |
| 2. | PV to DC bus | SISO | I | OFF | ON | OFF | ↑ | ↑ | - | ON | OFF | ↑ | ↑ | - | Boost |
| | | | II | OFF | OFF | ON | ↓ | ↓ | ↑ | ON | ON | ↓ | ↓ | ↑ | |
| 3. | Battery and PV to DC bus | DISO | I | ON | OFF | ON | ↑ | ↑ | ↑ | OFF | ON | ↓ | ↓ | - | Boost |
| | | | II | OFF | ON | ON | ↑ | ↓ | ↑ | ON | OFF | ↑ | ↓ | ↑ | |
| | | | III | OFF | ON | OFF | ↓ | ↑ | ↓ | ON | OFF | ↓ | ↑ | ↓ | |
| | | | IV | ON | OFF | ON | ↑ | ↓ | ↑ | OFF | ON | ↑ | ↓ | ↓ | |
| 4. | PV to DC bus and Battery | SIDO | I | OFF | ON | OFF | ↑ | ↑ | ↑ | ON | OFF | ↑ | ↑ | - | Buck and Boost |
| | | | II | ON | OFF | ON | ↓ | ↓ | ↓ | OFF | ON | ↓ | ↓ | ↑ | |
| 5. | DC bus to Battery | SISO | I | OFF | OFF | ON | ↑ | ↑ | - | ON | ON | ↑ | ↑ | ↑ | Buck |
| | | | II | ON | OFF | OFF | ↓ | ↓ | ↑ | OFF | OFF | ↓ | ↓ | ↓ | |

↑- Charging of inductor and capacitor, ↓- Discharging of inductor and capacitor
**ON**- Switch ON Position, **OFF**- Switch OFF Position

*3.6 Efficiency Calculation and Power Loss Analysis*

To determine converter efficiency, loss analysis is computed. While designing, power loss calculation plays an important role in converters. Power losses are classified as conduction losses and switching losses. Based on achieving ZCS conditions, switching losses are completely invalidated in the converter.

$$P_{Q(Total\ loss)} = P_{Q(sw.Loss)} + P_{Q(cond.Loss)}$$

$$P_{Q(loss(cond))} = R_{ds(on)} \times I^2_{ds(rms)} \times D$$

$$P_{Q(loss(switch))} = \frac{V_s \times I_s \times (T_{on} + T_{on}) \times f_{sw}}{2}$$

Due to ZCS performance in converters, total diode losses are completely ignorable. Therefore,

$$P_{loss(Diode)} = V_{FD} \times I_{D(avg)}$$

The power loss of the magnetic components is divided into copper loss and core loss. Therefore, the total power loss is calculated as,

$$P_{Total(Loss)} = P_{Loss(Sw)} + P_{D(Loss)} + P_{cap(Loss)} = 10.51\ \text{W}$$

Due to power losses delivered, the maximum peak efficiency of the topology observed at mode 3 can be represented as,

$$\eta(\%) = \frac{P_{out}}{P_{out} + P_{loss}} = \frac{150}{150 + 10.51} = 93.67\%$$

4. PROPOSED SYSTEM CONTROL STRATEGY

The system's five operating modes were explained through a flowchart as depicted in Fig.11. A proper control algorithm is implemented for switch duty ratios to govern load voltage, PV voltage, and the battery state, respectively. Here, three actively controlled switches, $S_1$, $S_2$, and $S_3$, are operated during different operating modes. $S_1$, $S_3$ are controlled to manage both battery and DC bus voltage through the PID controller. The switch $S_2$ is controlled through the conventional INC method to achieve MPPT, which measures the output of the PV module by providing surplus potential to charge the battery and load simultaneously. The flowchart of the Incremental Conductance algorithm of the PV system is shown in Fig.12.

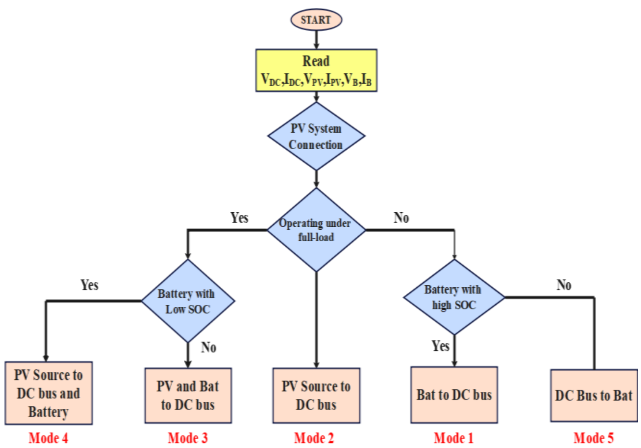


Fig. 11. Flowchart for Mode Selection.

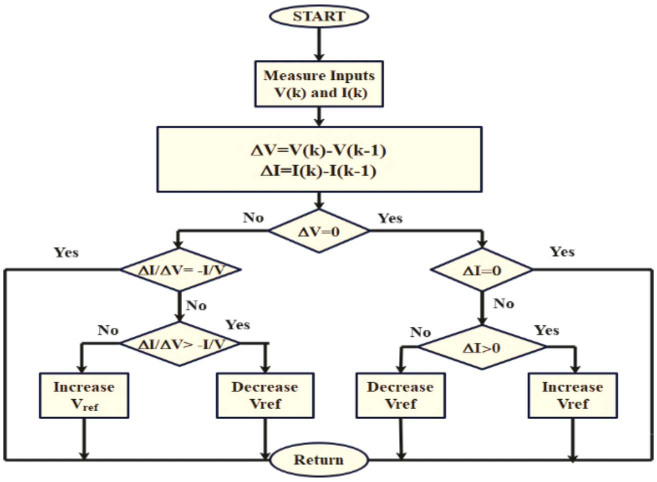


Fig. 12. Flowchart for Incremental Conductance (INC) Algorithm.

In mode 1, the converter receives PWM signals through the controller and operates in buck mode. In mode 2, the converter receives PWM pulses in boost mode, whereas PV power is only available to supply enough power. In modes 3 and 4, all the switches receive PWM signals to opérate both in buck and boost modes. In mode 5, RB action takes place from the load to sources, and the topology operates in buck mode. These modes are decided based on load demand and the available energy. The system is realized with controlled switches (MOSFET) and uncontrolled switches (diodes). A proper switching strategy is needed for each mode to achieve a seamless transition.

The block diagram of the proposed converter is portrayed in Fig. 13. Each process is determined by the PV voltage sensing, battery sensing, and DC bus voltage sensing. A conventional strategy PID controller is carried out for the proposed converter to regulate the output voltage under various load changing transitions. Based on the trial-and-error tuning method, an error signal is generated from the difference between the load voltage and the reference voltage. By repeating the tuning process and gains, it sets a desired output to generate the duty cycle for switches $S_1$ and $S_3$. The proposed converter is implemented using the PIC16FF811A controller.

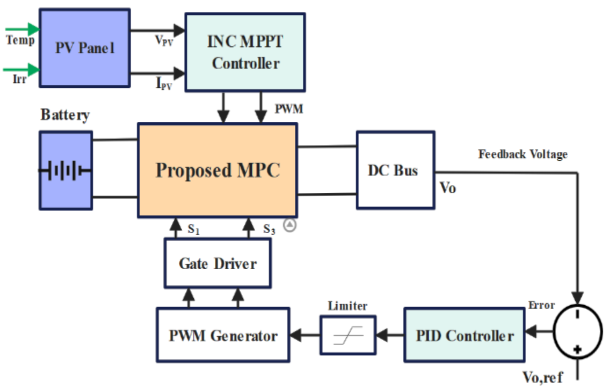


Fig. 13. Control Block Diagram of Proposed MPC.

The transition between each mode is enabled through the available energy among terminals. In mode 1, the PV power is not available because of heavily shaded conditions, so that only $S_1$ and $S_3$ are operated to transfer power from the battery to the DC bus, respectively. The switching strategy optimizes the proposed system and also manages the control objectives of the converter. According to the flow chart, each mode selection is described in five scenarios as follows:

*(i) PV power contribution:* In this scenario, due to the non-availability of PV power, only the battery with a high SOC can supply the required power to the load. The system remains OFF state at the battery's discharge limit.

*(ii) Without battery contribution:* In this scenario, MPPT is activated so that the PV source is enough to supply maximum power to the load and also charge the battery. When the PV is under MPPT, the system remains shut down.

*(iii) PV power and battery > DC Load power:* In this scenario, the PV module provides adequate energy to the load, while the battery supplies the remaining power.

*(iv) PV power> battery and DC Load power:* This scenario shows that solar power is enough to provide sufficient energy to the load and battery. To harness maximum power in PV panels, MPPT is activated.

*(v) DC Load > battery*: In this scenario, the system acts as a bi-directional converter to feed back energy from the DC bus (Load) to the battery.

## 5. SIMULATION RESULTS AND PERFORMANCE COMPARISON WITH EXISTING CONVERTERS

The comparison of converter output gain at different duty ratios with other existing topologies is illustrated in Fig. 14.

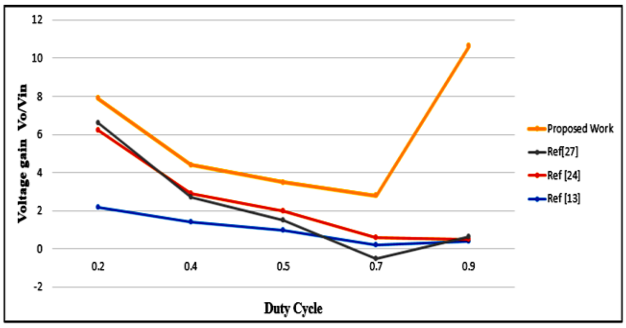


Fig. 14. Gain comparison with existing configurations.

The configuration performance and characteristics in terms of semiconductor components count, output gain, and converter efficiency are summarized in Table 3. On comparing with the other existing configurations, the proposed topology reaches maximum efficiency. The advantage of the converter is that it achieves fully soft switching conditions under all operating modes.

The specifications of the PV system are presented in Table 4, and the simulation parameters are shown in Table 5.

The simulation results are executed using MATLAB 2022a toolbox under various modes, as shown in Table 6. Fig. 15 shows the simulated output voltage of 24V, and Fig. 16 represents the output current of 20mA at mode 1 (Battery to DC bus). The switching pulse generation of a 0.6 duty cycle range is depicted in Fig. 17, respectively.

**Table 3. Proposed system comparison table with existing literatures.**

| Reference | Structure | No. of Magnetic cores | No. of Capacitors | Voltage Gain | No. of switches used | Switching frequency | Power | Efficiency |
|---|---|---|---|---|---|---|---|---|
| [2] |  | 4 | 5 | $\frac{2+n_3D+n_2(1-D)}{1-2D}$ | 2 | 100KHz | 200 W | 90% |
| [7] |  | 4 | 4 | $\frac{2}{(1-D)^2}$ | 4 | 50KHz | 250 W | 93.1% |
| [13] | 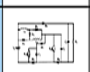 | 2 | 3 | $\frac{(3-D)}{1-3D}$ | 2 | 50KHz | 200 W | 88.6% |
| [24] |  | 2 | 3 | $\frac{(1-D)}{D}$ | 3 | 50KHz | 100 W | 93.4% |
| [27] | 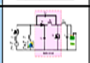 | 4 | 3 | $\frac{(1-D)}{(1-2D)}$ | 2 | 20KHz | 100 W | 91.5% |
| Proposed Work |  | 3 | 3 | $\frac{(1-D)}{(1-D)^2}$ | 3 | 20KHz | 100W | 93.67% |

**Table 4. PV Module Specifications.**

| Parameters (Loom solar) | Ratings |
|---|---|
| Maximum power Voltage ($V_{mp}$) | 19.95 V |
| Maximum power current ($I_{mp}$) | 2.51 A |
| Maximum Power ($P_{max}$) | 50 Wp |
| Short circuit current ($I_{sc}$) | 2.63 A |
| Open circuit voltage ($V_{oc}$) | 12 V,1.3 Ah |

**Table 5. Specifications of Simulation Parameters.**

| Parameters | | Simulation Values |
|---|---|---|
| Input Voltage ($V_{in}$) | Mode 1 | 12V |
| | Mode 2 | 33 V |
| | Mode 3 | Battery-12 V, PV-33 V |
| | Mode 4 | 33V |
| | Mode 5 | 20 V |
| Duty Cycle | | 0.5 |
| Switching Frequency | | 20kHz |
| Inductors | | $L_1=L_2=L_3=150$ mH |
| Capacitors | | $C_1=C_2=20\mu F$ <br> $C_o=100\mu F$ |
| Load Resistance | | 1kΩ |
| Battery Range | | 12 V,1.3 Ah |

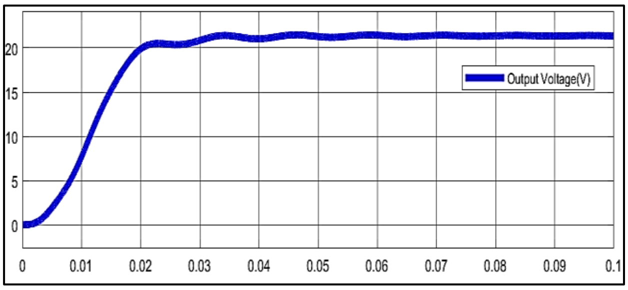


Fig. 15. Simulation waveform of output voltage.

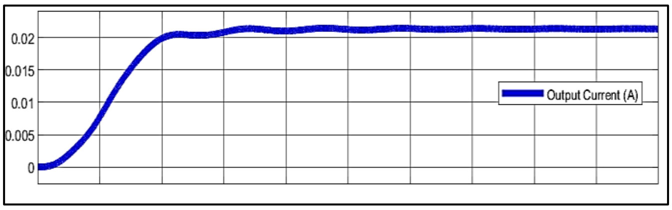


Fig. 16. Simulation waveform of output current.

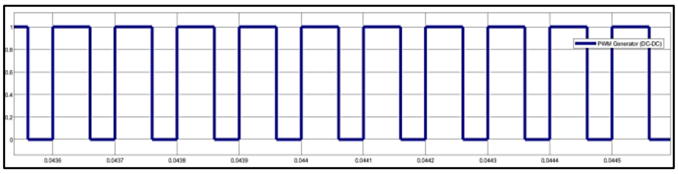

Fig. 17. Switching pulse generation.

The simulation of its battery characteristics is shown in Fig. 18. Here, SOC shows that the battery starts discharging from its initial state (80%) to supply enough power to the DC bus (Load). The observed ZCS waveform is represented in Fig. 19.

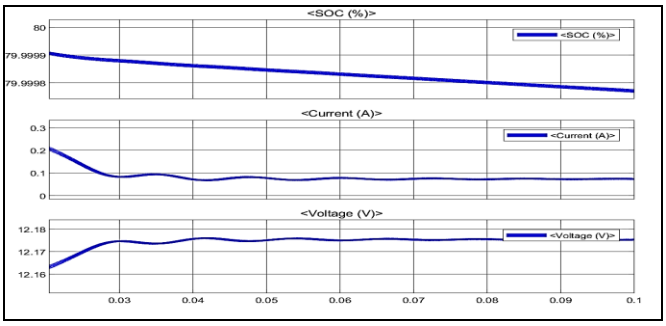


Fig. 18. Battery characteristics.

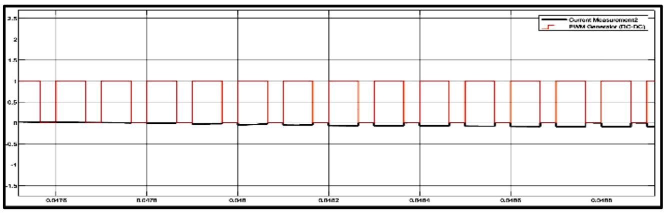

Fig. 19. ZCS Waveform.

With PV input voltage of 34V shown in Fig. 20, and Fig. 21 represents the ripple-less load current and its obtained output voltage waveform of 38V at mode 4 (PV to Battery and DC bus) is represented in Fig. 22. It is proven that the battery starts charging from its initial state, and its response characteristics are presented in Fig. 23. The switching pulse generation at 0.6 duty cycle range and the obtained ZCS waveform in this mode is represented in Fig. 24, respectively. The period gradually occurs at zero current to make a continuous output current.

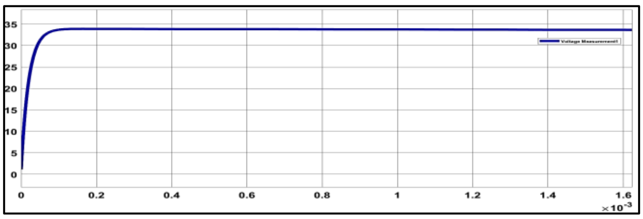

Fig. 20. PV system input voltage.

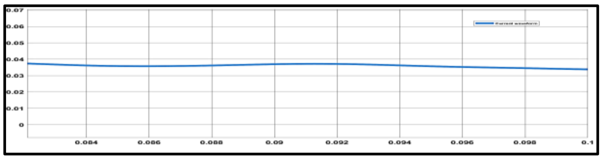

Fig. 21. Output load current of mode 4.

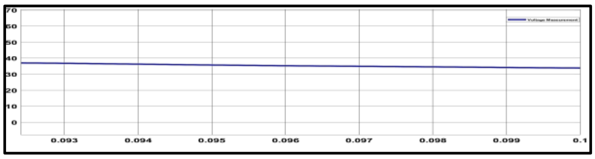

Fig. 22. Output load voltage of mode 4.

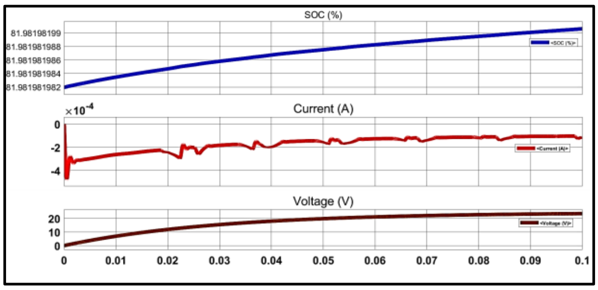


Fig. 23. Battery characteristics.

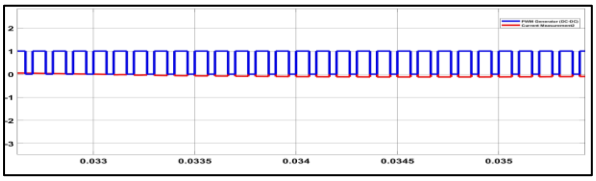

Fig. 24. ZCS waveform.

**Table 6. Simulation results of the proposed topology.**

| S. No | Modes | Input Voltage ( $V_{in}$) | Duty cycle | Output Voltage ($V_o$) | Output Power ($P_o$) | η (%) | Status |
|---|---|---|---|---|---|---|---|
| 1. | Battery to DC Bus | 12V | 0.5 | 24 V | 48 W | 85.6 % | Buck |
| 2. | PV to DC Bus | 33 V | 0.6 | 40.6 V | 60 W | 87.2% | Boost |
| 3. | Battery and PV to DC Bus | Battery- 12 V PV- 33 V | 0.7 0.7 | 40V | 56W | 93.67% | Boost |
| 4. | PV to DC Bus and Battery | 33 V | 0.6 | 33 V | 12.6 W | 72% | Buck and Boost |
| 5. | DC Bus to Battery | 20 V | 0.7 | 22 V | 10 W | 81% | Buck |

## 6. EXPERIMENTAL RESULTS

To validate the configuration performance and effectiveness, a hardware prototype of 150W was designed, built, and developed in the laboratory. The experimental setup and the hardware prototype are shown in Fig. 25 and Fig. 26. The hardware specifications are presented in Table 7.

An incremental conductance (INC) algorithm is incorporated to harness maximum power from the panel where $V_{mp}$=19.5V. The battery and PV sources are configured as input ports, and the output port is configured at varying load resistances.

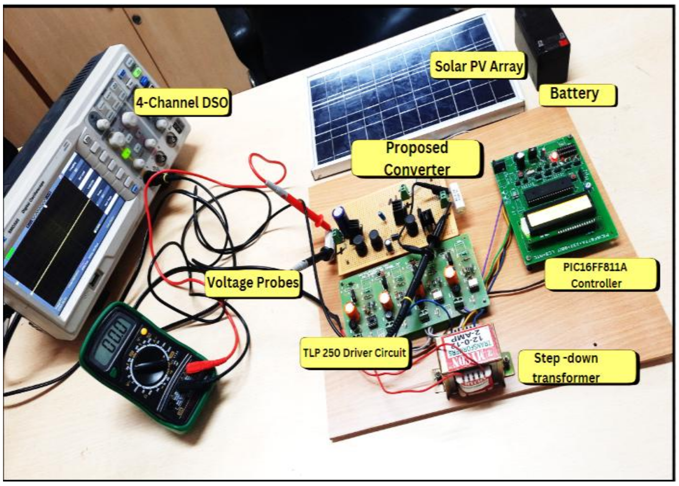


Fig. 25. Experimental setup of the proposed configuration.

The transition waveforms of various modes are demonstrated in the following waveforms. Each waveform represents PV voltage, battery voltage, and output DC bus voltage under load resistances (1kΩ, 10kΩ), respectively.

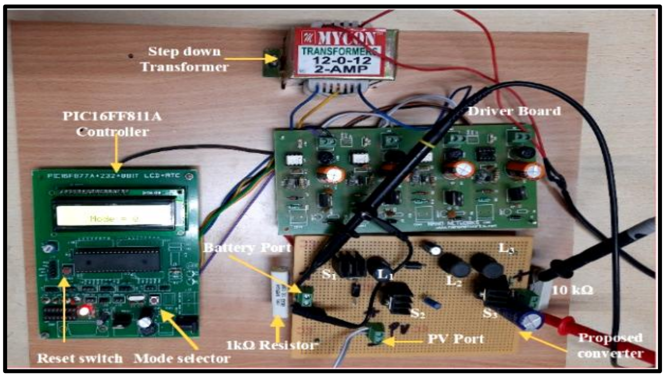


Fig. 26. Hardware prototype of the proposed system.

**Table 7. Specifications of the hardware prototype.**

| Parameters | Experimental Value |
|---|---|
| PV Panel | Loom solar, 24V,2.5 A |
| Input Voltage ($V_{in}$) | 6V (Mode 1)<br>12.4 V (Mode 2)<br>11.20 V (Mode 4 ) |
| Duty Cycle | 0.5 |
| Switching Frequency | 20 kHz |
| Inductors | $L_{PV}$, $L_R$= $L_3$=100 mH |
| Battery Range | 12 V,1.3 Ah |
| Capacitors | $C_1$=10 µF,50 V,<br>$C_R$=22µF,100 V,<br>$C_o$=100µF,250 V |
| Controller | PIC16FF811A |
| MOSFETs | IRF630 |
| Load Resistance | 1kΩ, 10kΩ |

The PIC16FF811A controller is implemented to generate switching pulses in all modes at a 20 kHz switching frequency. The PWM pulse generation for $S_1$ and $S_3$ in mode 1 (battery mode) is shown in Fig. 27 at a 60% duty ratio. This mode can operate in a buck state and maintains ripple-less load current as shown in Fig. 28. In PV mode (mode 2), the generated pulses at 50% duty ratio and boosted load voltage are shown in Fig. 29 and Fig. 30. Similarly, the switching pulses generation of mode 3 in four states are shown in Fig. 31, and the output load voltage is shown in Fig. 32. The system is also tested for variation of load resistance from 1kΩ to 10kΩ as shown in Fig. 33. It is evident from the figures, the converter operates at constant regulated output voltage and maintains ripple-less load current in all modes at 40% to 60% duty ratios satisfactorily under load variations. To evaluate the converter performance, the system operates at two different loads and achieves maximum efficiency of about 93.67% eminently at mode 3, referred to as PV and battery to the DC load.

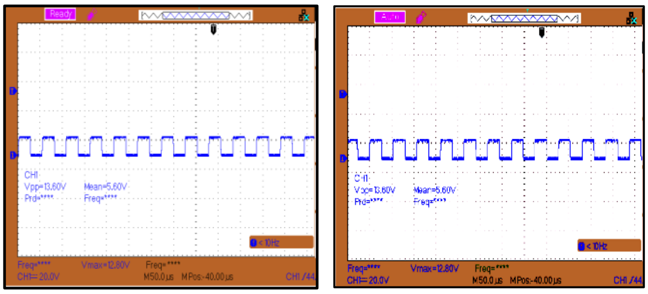

Fig. 27. Switching pulses generation of $S_1$ and $S_3$ in mode 1

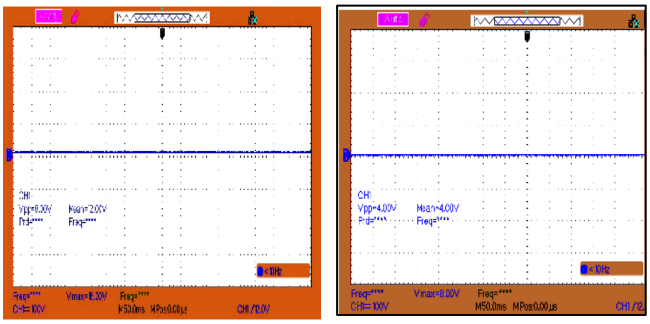

Fig. 28. Hardware result of input voltage and output voltage at mode 1 (Battery mode).

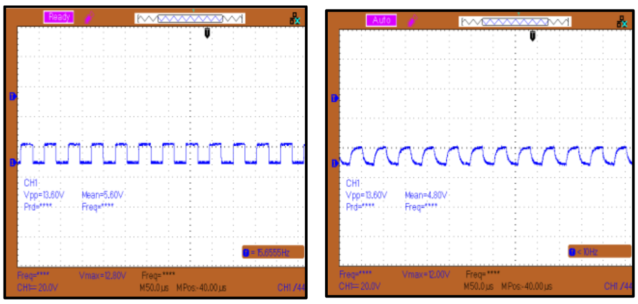

Fig. 29. Switching pulses generation for $S_2$ and $S_3$ in mode 2 (PV mode)

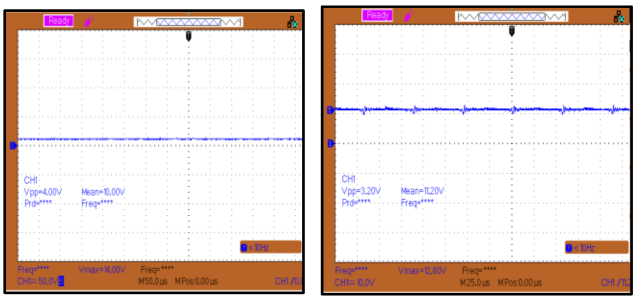

Fig. 30. Hardware result of input voltage and output voltage (PV mode).

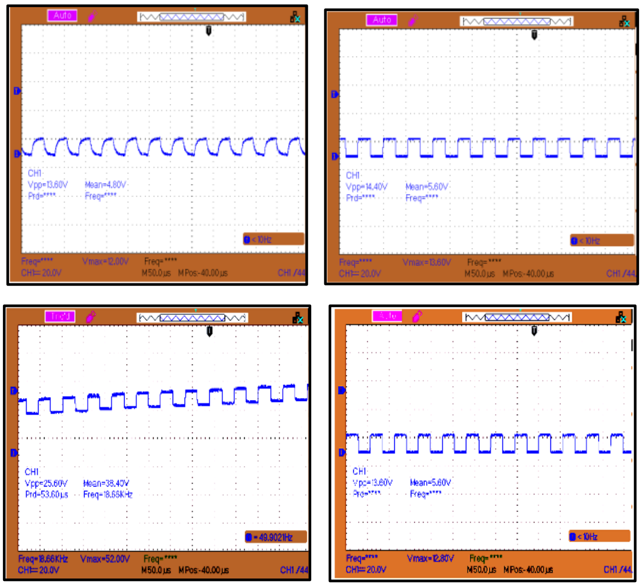

Fig. 31. Switching pulses generation for $S_1$, $S_2$, $S_3$ in four states.

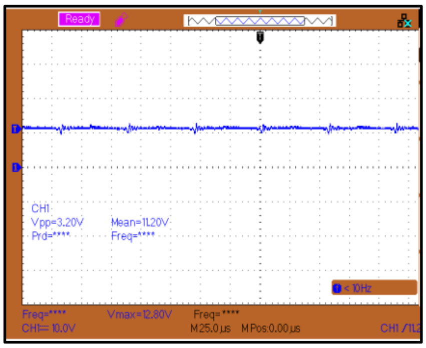

Fig. 32. Hardware result of load voltage at mode 3 with 1kΩ load resistance.

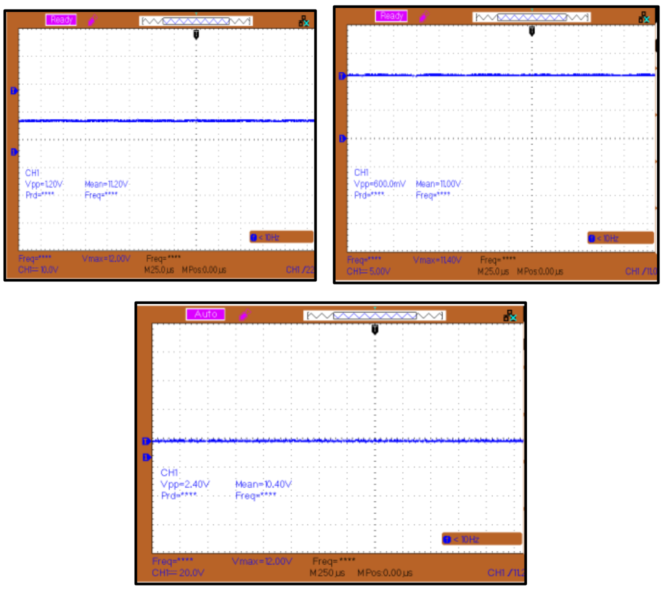

Fig. 33. Hardware result of source and load voltage at mode 3 due to variation in load at 10kΩ.

The performance curve plotted between efficiency versus voltage gain compared with other configurations is presented in Fig. 34. It is proven that the proposed topology achieves máximum efficiency than other existing systems.

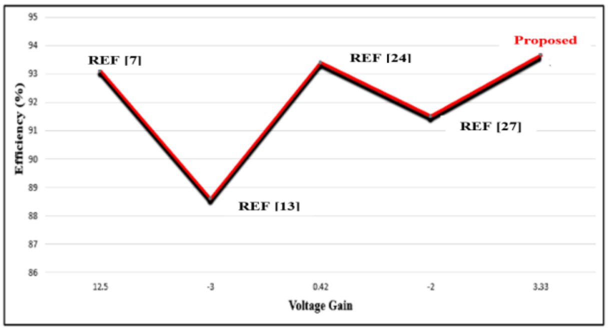


Fig. 34. Proposed converter efficiency versus voltage gain.

## 7. CONCLUSIONS

This article introduced a soft-switching multiport Converter (MPC) that features a switched Z-Quasi Resonant (S-ZQR) network utilizing dual sources such as a PV system and a battery. Operating without any auxiliary circuit, the topology can operate in five modes and achieve ZCS conditions by maintaining continuous load current. The modes of operation, theoretical analysis, design guidelines, and key waveforms are reported in detail. The simulation results of all modes are executed using the MATLAB/Simulink software.

Later, a brief comparison of the converter performance with existing systems was carried out in terms of component count, duty ratio, converter gain, and efficiency. An experimental prototype of 150W was built, tested, and validated with the theoretical and simulation results. Therefore, the proposed configuration achieves a maximum efficiency of 93.67% under load variations and maintains constant voltage regulation.

Finally, it is concluded that the system has improved efficiency using fewer components, and hence it is suggested to be applicable for auxiliary loads in electric vehicles and DC micro-grids applications. The future scope of this work is to be further extended for electric vehicle charging systems.

## REFERENCES

Ali, H. H. H. Mousa, M. F. Shaaban, M. A. Azzouz and A. S. A. Awad, (2024). A Comprehensive Review on Charging Topologies and Power Electronic Converter Solutions for Electric Vehicles. *Journal of Modern Power Systems and Clean Energy*, vol. 12, no. 3, pp. 675-694.

Abbasian S, H. S. Gohari, M. Farsijani, K. Abbaszadeh, H. Hafezi and S. Filizadeh, (2022). Single-Switch Resonant Soft-Switching Ultra-High Gain DC-DC Converter With Continuous Input Current. *IEEE Access*, vol. 10, pp. 33482-33491.

Alajmi N, M. I. Marei and I. Abdelsalam,(2021). A Multiport DC–DC Converter Based on Two-Quadrant Inverter Topology for PV Systems. *IEEE Transactions on Power Electronics*, vol. 36, no. 1, pp. 522-532.

Aljarajreh H, D. D. -C. Lu, Y. P. Siwakoti and C. K. Tse, (2022). A Nonisolated Three-Port DC–DC Converter With Two Bidirectional Ports and Fewer Components. *IEEE Transactions on Power Electronics*, vol. 37, no. 7, pp. 8207-8216.

Bao, A. Kumar, X. Pan, X. Xiong, A. R. Beig and S. K. Singh, (2021). "Switched Inductor Double Switch High Gain DC-DC Converter for Renewable Applications. *IEEE Access*, vol. 9, pp. 14259-14270.

Cheng X.F, C. Liu, D. Wang and Y. Zhang, (2021). State-of-the-Art Review on Soft-Switching Technologies for Non-Isolated DC-DC Converters. *IEEE Access*, vol. 9, pp. 119235-119249.

de Carvalho M.R.S, E. A. O. Barbosa, F. Bradaschia, L. R. Limongi and M. C. Cavalcanti, (2022). Soft-Switching High Step-Up DC–DC Converter Based on Switched-Capacitor and Autotransformer Voltage Multiplier Cell for PV Systems. *IEEE Transactions on Industrial Electronics*, vol. 69, no. 12, pp. 12886-12897.

Fang Z, Z. Wei, Z. Huang and F. Liu, (2021). Onboard Energy Storage System Based on Interleaved High-Conversion-Ratio Quasi-Resonant Converter With Small Characteristic Impedance. *IEEE Transactions on Vehicular Technology*, vol. 70, no. 5, pp. 4238-4251.

Faraji R, L. Ding, T. Rahimi, M. Kheshti and M. R. Islam, (2021). Soft-Switched Three-Port DC-DC Converter With Simple Auxiliary Circuit. *IEEE Access*, vol. 9, pp. 66738-66750.

Hassanpour N, A. Chub, A. Blinov and D. Vinnikov,(2023). Soft-Switching Bidirectional Step-Up/Down Partial Power Converter With Reduced Components Stress. IEEE Transactions on Power Electronics, vol. 38, no. 11, pp. 14166-14177.

Heidari M, M. Esteki, S. A. Khajehoddin and H. Farzanehfard,(2022)"A High Voltage Gain ZVT Quasi-Z-Source Converter With Reduced Voltage Stress," in *IEEE Transactions on Power Electronics*, vol. 37, no. 11, pp. 13696-13710.

He L and X. Xu, (2022). Soft-Switching Bidirectional Switched-Capacitor DC–DC Converter With Multiple Phase Shift Control Methods. *IEEE Journal of Emerging and Selected Topics in Power Electronics*, vol.10,no.2,pp.1537-1547.

Kim Y B, B. -S. Lee, S. -H. Lee, J. -H. Ahn and J. -K. Kim, (2021). Integrated Single Inductor Converter for a DC Grid System Connected With Battery and Load. *IEEE Transactions on Industrial Electronics*, vol. 68, no. 12, pp. 12010-12020.

Kothapalli K R, M. R. Ramteke, H. M. Suryawanshi, N. K. Reddi and R. B. Kalahasthi, (2021). Soft-Switched Ultrahigh Gain DC–DC Converter With Voltage Multiplier Cell for DC Microgrid. *IEEE Transactions on Industrial Electronics*, vol. 68, no. 11, pp. 11063-11075.

Li Y and G. J. Kish,(2022). Comparative Assessment of Multi-Port MMCs for High-Power Applications. *IEEE Access*, vol. 10, pp. 22049-22060.

Maalandish, M., Hosseini, S.H., Sabahi, M., Rostami, N., Khooban, M.-H. (2024). Soft-switching multiport DC-DC converter for PV/EV applications with a bidirectional port. *IET Renew. Power Gener.* 1–18.

Maghsoudi M and H. Farzanehfard, (2024). Fully Soft-Switched Buck–Boost Bridgeless PFC Converters With Single-Magnetic Core. *IEEE Transactions on Industrial Electronics*, vol. 71, no. 1, pp. 419-426.

Moumita Das (2023). Review of the Wide-Input-Wide-Output Bi-directional DC-DC Converter for Electric Vehicle Applications. *IETE Technical Review*, 41(1),85-97.

Mudadla Dhananjaya & Swapnajit Pattnaik (2022). Review on Multi-Port DC–DC Converters. *IETE Technical Review*, 39:3, 586-599.

Patakamoori, R. R. Udumula, T. K. Nizami and K. R. R. Ch, (2023). An Efficient Soft-Switched LED Driver for Street Lighting Applications With Input Regulation. *IEEE Journal of Emerging and Selected Topics in Power Electronics*, vol. 11, no. 5, pp. 5018-5028.

Rostami S, V. Abbasi and N. Talebi, (2022). Ultrahigh Step-Up Multiport DC–DC Converter With Common Grounded Input Ports and Continuous Input Current. *IEEE Transactions on Industrial Electronics*, vol. 69, no. 12, pp. 12859-12873.

Shameli, M. Maghsoudi and H. Farzanehfard, (2024). Bridgeless Cuk PFC Converter With Soft Switching in Full Input Voltage and Load Range. *IEEE Transactions on Industrial Electronics*, vol. 71, no. 7, pp. 6938-6945.

Talebi P, M. Packnezhad and H. Farzanehfard, (2023). Fully Soft-Switched Ultra-High Step-Up Converter With Very Low Switch Voltage Stress. *IEEE Transactions on Power Electronics*, vol. 38, no. 3, pp. 3523-3530.

Tian G, S. Chen, X. Ding, J. Peng and Z. Kou, (2024). Isolated High Step-Up Soft-Switching Quasi-Z-Source DC–DC Converter. *IEEE Access*, vol. 12, pp. 49927-49936.

Wang Z, P. Wang, B. Li, X. Ma and P. Wang (2021). A Bidirectional DC–DC Converter With High Voltage Conversion Ratio and Zero Ripple Current for Battery Energy Storage System. *IEEE Transactions on Power Electronics*, vol. 36, no. 7, pp. 8012-8027.

Wang J, K. Sun, C. Xue, T. Liu and Y. Li (2022). Multi-Port DC-AC Converter With Differential Power Processing DC-DC Converter and Flexible Power Control for Battery ESS Integrated PV Systems. *IEEE Transactions on Industrial Electronics*, vol. 69, no. 5, pp. 4879-4889.

Yuan F, R. Hao, X. You and P. Xiang, (2023). A High Voltage Gain Soft-Switching Bidirectional DC-DC Converter With Wide Range Using Resonant Network. *IEEE Transactions on Power Electronics*, vol. 38, no. 11, pp. 14099-14114.

Zareie M, B. Poorali, S. Eren and M. Pahlevani, (2021). New DC–DC Converter With Direct Power Transfer Capability. *IEEE Transactions on Power Electronics*, vol. 36, no. 5, pp. 5647-5663.

Zhang H, D. Dong, M. Jing, W. Liu and F. Zheng, (2022). Topology Derivation of Multiple-Port DC–DC Converters Based on Voltage-Type Ports. *IEEE Transactions on Industrial Electronics*, vol. 69, no. 5, pp. 4742-4753.

Zhang Y, S. Gao, S. Jing and X. Huang, (2023). Soft-Switching Operation With a Variable Switching Frequency Control for Switched-Quasi-Z-Source Bidirectional DC–DC Converter in EVs. *IEEE Transactions on Industrial Electronics*, vol. 70, no. 1, pp. 384-395.